


## Original Paper

# Synthesis and photocatalytic activity of montmorillonite/TiO<sub>2</sub> nanocomposites for rhodamine B degradation under UVC irradiation

Bang Tam Thi Dao<sup>1,3</sup> , Thu Loan Thi Ha<sup>1,3</sup>, Trung Do Nguyen<sup>1,3</sup>, Hon Nhien Le<sup>1,3</sup>, Tien Trung Vu<sup>1,3</sup>,  
Huu Truong Nguyen<sup>2,3</sup> and Chi-Nhan Ha-Thuc<sup>1,3</sup> 

<sup>1</sup>Faculty of Materials Science and Technology, University of Science, Ho Chi Minh City, Vietnam; <sup>2</sup>Laboratory of Advanced Materials, University of Science, Ho Chi Minh City, Vietnam and <sup>3</sup>Vietnam National University, Ho Chi Minh City, Vietnam

## Abstract

The increasing contamination of water by organic dyes causes water pollution in the environment. Factories discharge untreated effluents into nearby water courses adding to the existing water pollution; this poses a significant environmental challenge. Hence there is a pressing demand to develop efficient technology for wastewater treatment, and photocatalysis has emerged as an advanced oxidation process with a green chemical approach for such treatment. This study aims to synthesize montmorillonite/TiO<sub>2</sub> (Mnt/TiO<sub>2</sub>) photocatalysts and clarify the effect of montmorillonite content on the photodegradation of the organic dye rhodamine B (RhB). Mnt/TiO<sub>2</sub> was prepared by a chemical method with various mass ratios of  $m_{\text{Mnt}}:m_{\text{TiO}_2}$  based on the cation exchange capacity (CEC) of Mnt. The physicochemical properties of the samples prepared were determined by the following methods: energy-dispersive X-ray spectroscopy (EDX), scanning electron microscopy (SEM), Brunauer–Emmett–Teller (BET), X-ray diffraction (XRD), and Fourier transform infrared spectroscopy (FTIR). The photocatalytic degradation efficiency of the RhB solution of Mnt/TiO<sub>2</sub> was investigated by UV-Vis spectroscopy under UVC irradiation. Liquid chromatography-mass spectrometry (LCMS) was used to identify the photocatalytic by-products. The results showed that the structure of the nanocomposites has a ‘house-of-cards’ form with TiO<sub>2</sub> nanoparticles randomly distributed on the surface and sheets of clay minerals. The best mass ratio of  $m_{\text{Mnt}}:m_{\text{TiO}_2}$  is 10:1, corresponding to a 10 ppm RhB solution decolorization efficiency of 91.5% in 210 min. In this study, Mnt/TiO<sub>2</sub> successfully cleaved the dye chromophore structure and broke the RhB rings into small and broken-ring compounds.

**Keywords:** adsorption; montmorillonite/TiO<sub>2</sub> nanocomposites; organic dye; photocatalyst; rhodamine B; treatment of waste water

(Received: 05 January 2024; revised: 28 May 2024; accepted: 19 June 2024)

## Introduction

The development of the textile industry has many benefits. However, along with that development, people risks the environment becoming polluted by wastewater from industry, chemical factories, textile dyeing, etc. Azo dyes are utilized widely, primarily because of their low cost and significant color fastness (Hassan Alzain et al., 2023). Aromatic amines, the primary by-products of untreated azo dyes released into the environment, have been classified as compounds with significant potential to induce cancer, genetic mutations, and ecological imbalance (Rania Al-Tohamy et al., 2022). Traditional methods of solving problems related to water treatment can be costly and cause secondary pollution (Chengyue et al., 2022; Muhammad et al., 2022; Yanmin et al., 2022). Therefore, it is urgent to research and manufacture

advanced materials that can treat environmental pollutants effectively. ‘Bleaching’ refers to the process of using chemicals or other agents to lighten or remove color from a material. Meanwhile, ‘mineralization’ refers to the process by which organic matter is converted into minerals. Mineralization of dyes typically refers to the degradation or breakdown of dye molecules into simpler, inorganic compounds. This process can metabolize or break down complex organic molecules such as dyes. The result of mineralization is the conversion of these organic dye molecules into inorganic end products. In the context of environmental science and waste-water treatment, the mineralization of dyes is important for reducing the environmental impact of dye-containing effluents. When dyes are released into water bodies or waste water, their persistence can be harmful. Mineralization processes play a role in breaking down these dyes into less harmful or inert substances, reducing the color and potential toxicity of the effluent. Recently, photocatalysis has been considered an effective solution to the problems above (Henrique et al., 2010; Tammanoon et al., 2021). Natural clays such as montmorillonite (Mnt), zeolite, kaolinite, and vermiculite with a porous structure, large surface area, and significant cation

**Corresponding author:** Chi-Nhan Ha-Thuc; Email: [htcnhan@hcmus.edu.vn](mailto:htcnhan@hcmus.edu.vn)

**Cite this article:** Dao B.T.T., Ha T.L.T., Nguyen T.D., Le H.N., Vu T.T., Nguyen H.T., & Ha-Thuc C.-N. (2024). Synthesis and photocatalytic activity of montmorillonite/TiO<sub>2</sub> nanocomposites for rhodamine B degradation under UVC irradiation. *Clays and Clay Minerals* 72, e22, 1–14. <https://doi.org/10.1017/cmn.2024.25>

exchange capacity (CEC) have attracted much attention in recent years due to their potential applications in many different fields (Miao *et al.*, 2006; Ke *et al.*, 2010; Zhaohui *et al.*, 2018). Mnt is an aluminosilicate clay with a 2:1 layer structure, which can adsorb organic substances on the surface or in the space between its sheets by interacting or replacing exchangeable cations (Neelaveni *et al.*, 2019; Bang Tam *et al.*, 2021; Xinyu *et al.*, 2021; Bang Tam *et al.*, 2022; Bang Tam *et al.*, 2023). However, Mnt has a disadvantage: it will reverse to desorption to the medium when the adsorption equilibrium is reached. Therefore, the ability to modify Mnt to improve and enhance the adsorption capacity is needed urgently at present (Alireza *et al.*, 2016; Alireza *et al.*, 2017). Titanium dioxide (TiO<sub>2</sub>) pillared montmorillonite (PILM) was synthesized successfully by impregnating a TiO<sub>2</sub> sol into the interlayers of Mnt using TiCl<sub>4</sub> as the precursor of TiO<sub>2</sub> (Gao *et al.*, 2018). However, the effect of Mnt content on photocatalytic efficiency has not been studied. Due to their many exciting properties, porous heterostructures based on TiO<sub>2</sub> and clay minerals have attracted more attention. These nanocomposites can be used as photocatalysts to treat waste water contaminated by toxic organic compounds (Ewa *et al.*, 2021; Kelechi *et al.*, 2021; Joanna *et al.*, 2022).

Several recent studies have investigated the synthesis of TiO<sub>2</sub>-clay composites using various methods, e.g. Aydin *et al.* (2018) synthesizing TiO<sub>2</sub>/Mnt nanocomposites by a simple hydrothermal method with tetraethyl orthotitanate as a precursor of Ti. The TiO<sub>2</sub>/Mnt was applied as a catalyst for the sonocatalytic degradation of ciprofloxacin. Under the following conditions, pH 6, catalyst dosage of 0.2 g L<sup>-1</sup>, initial CIP concentration of 10 mg L<sup>-1</sup>, and ultrasonic power of 650 W L<sup>-1</sup>, a degradation efficiency of 65.01% was obtained (Aydin *et al.*, 2018). Jiao *et al.* (2018) prepared TiO<sub>2</sub>-pillared Mnt nanocomposites (TM) from Mnt with tetrabutyl titanate by a sol-gel method. The samples were placed in a chamber for 336 h under a 500 W UV lamp. Although the exposure time is long and the radiation power is high, the degradation efficiency is only 55% (Aydin *et al.*, 2018). Amit *et al.* (2017) synthesized bentonite clay-based TiO<sub>2</sub> with titanium (IV) butoxide under microwave conditions to degrade methylene blue under a 64 W UV lamp. The greatest degree of photocatalytic activity was achieved using bentonite containing 50% TiO<sub>2</sub> by weight because of its relatively large specific surface area and pore volume (Amit *et al.*, 2017). hydrothermally with tetrabutyl titanate for use as photocatalysts for methylene blue degradation at various pH values, reaction temperatures, and dwelling times; 30% TM achieved a methylene-blue removal efficiency of 95.6% (Yonghui *et al.*, 2022). Many previous studies have prepared TiO<sub>2</sub>-clay nanocomposites by impregnating TiO<sub>2</sub> either on the clay surface or between its layers with various precursors, such as titanium isopropoxide, titanium (IV) butoxides, titanyl sulfate (TiOSO<sub>4</sub>) or titanium tetrachloride (TiCl<sub>4</sub>) (Aydin *et al.*, 2017; Kelechi *et al.*, 2021).

The difference in this study compared with previous studies is that the Mnt was denatured with TiO<sub>2</sub> anatase (Merck) by a simple wet stirring method without annealing temperature. Mnt is purified from bentonite (Vietnam) by a chemical method (patented by the Intellectual Property Office of Vietnam with code B071-2013-02346 SC in 2017). Previous studies have not adequately explored how the Mnt content in nanocomposites affects photocatalytic degradation efficiency. Moreover, research on the photocatalytic degradation of azo-based organic dyes, such as rhodamine B (RhB), remains limited. This present study addressed these gaps by demonstrating a method that achieves high degradation efficiency of azo-organic dyes while minimizing the intermediate chemicals required in the synthesis process. Additionally, the Mnt/TiO<sub>2</sub> nanocomposite developed in

this study is anticipated to achieve high photodegradation efficiency with reduced contact time and lower excitation source power compared with existing methods.

## Materials and methods

### Materials

The present study used TiO<sub>2</sub> (Merk KgaA, Germany; anatase phase), rhodamine B (Sigma-Aldrich, Singapore), bentonite (Lam Dong Province, Vietnam), ethanol (Merck KgaA, Germany), and NaCl (Merck KgaA, Germany).

### Preparation of Mnt

The Mnt-purification steps in this study were similar to those used in previous studies (Ha Thuc *et al.*, 2010; Nguyen Van *et al.*, 2020; Bang Tam *et al.*, 2021, Bang Tam *et al.*, 2022; Bang Tam *et al.*, 2023). Bentonite was dispersed in water and stirred mechanically for 24 h. NaCl was then added and stirred mechanically for 3 h. The suspension was centrifuged and washed several times with deionized water and ethanol – the suspension was centrifuged and dried at 60°C for 72 h to obtain pure Mnt.

### Preparation of Mnt–TiO<sub>2</sub> nanocomposite

In this study, the amount of TiO<sub>2</sub> used was calculated based on the CEC of Mnt by Eqn (1) (Johannes *et al.*, 2019):

$$\text{Weight of TiO}_2(\text{g}) = n \times \text{CEC} \times A \times B, \quad (1)$$

where CEC is the cationic exchange capacity of Mnt (CEC = 0.00097 mol g<sup>-1</sup>; Ha Thuc *et al.*, 2010); *A* is the weight of Mnt (g); *B* is the molecular weight of TiO<sub>2</sub> (g mol<sup>-1</sup>); and *n* is the ratio to be used (Tushar and Bergaya, 2006).

The steps for synthesizing Mnt–TiO<sub>2</sub> nanocomposites were as in previous publications (Bang Tam *et al.*, 2021; Bang Tam *et al.*, 2022). Mnt was added slowly to 100 mL of deionized water and stirred until the Mnt was wholly dispersed in the solution. Nanocomposites of TiO<sub>2</sub> and Mnt were formed by stirring TiO<sub>2</sub> in Mnt suspension for 4 h with various mass ratios, *m*<sub>Mnt</sub>:*m*<sub>TiO<sub>2</sub></sub> = 10:1, 5:1, and 1:1; corresponding to the samples denoted MT10-1, MT5-1, and MT1-1. These mixtures were sonicated for 1 h. The products obtained were centrifuged and dried at 80°C for 24 h to form the Mnt–TiO<sub>2</sub> nanocomposites.

### Characterization

The elemental composition of the nanocomposites was determined by energy-dispersive X-ray spectroscopy (EDX; HORIBA H-7593, Hitachi, Japan). Scanning electron microscopy (SEM: S4800, Hitachi, Japan) was used to examine the samples' surface morphology. Crystal characteristics and bonding vibrations were analyzed by the following methods, respectively: X-ray diffraction analysis (XRD; D2 PHASER diffractometer, Bruker, Germany) with Ni-filtered CuK radiation (λ=1.540 Å) at 40 kV, 40 mA, scan rate 0.030° s<sup>-1</sup> and scan angle 5–80°2θ and Fourier transform infrared spectroscopy (FTIR; Nicolet iS 50 (ThermoFisher, USA) in the range from 4000 to 400 cm<sup>-1</sup>). Surface areas of Mnt and MT10-1 were analyzed using the Brunauer–Emmett–Teller (BET) method with N<sub>2</sub> adsorption-desorption isotherms at 77.3 K on the Nova 1000e (Quanta chrome) instrument (FL, USA). Their pore volume and diameter

were analyzed using the Barrett–Joyner–Halenda (BJH) method. The absorption and photocatalytic properties were measured with UV-Vis absorption spectroscopy (Jasco V-670, Tokyo, Japan). The by-products of RhB degradation were analyzed via the LCMS method (XEVO-TQD, Milford, MA, USA).

#### Adsorption/photocatalysis experimental set-up

The photocatalytic decomposition of Rhodamine B (RhB) was carried out in a closed system consisting of an excitation source (a UVC lamp; 254 nm, 15 W) placed 7 cm above the surface of the solution (Fig. 1). Initially, 10 mg of the photocatalyst was dispersed in 100 mL of 10 ppm RhB. Before turning on the UVC lamp, the mixture was stirred magnetically in the dark for 60 min to reach adsorption–desorption equilibrium. The solution was then irradiated by a UVC lamp for 210 min. The photocatalytic reaction occurred during this time. Every 30 min, 10 mL of solution was extracted and stored in centrifuge tubes.

The RhB adsorption experiment for 210 min was performed the same way as above but without UVC irradiation. The solution in the centrifuge tubes was centrifuged and measured with a UV-Vis spectrometer (Jasco V-670) in the 400–700 nm region, a step of 0.2 nm, and a scan rate of 400 nm min<sup>-1</sup>. Solution concentrations before and after adsorption/photocatalysis were used to calculate the decolorization efficiency using Eqn (2):

$$H = \left(1 - \frac{C}{C_0}\right) \times 100, \quad (2)$$

where  $H$  is the decolorization efficiency (%);  $C_0$  is the concentration of the RhB initially (mg L<sup>-1</sup>); and  $C$  is the concentration of the RhB (mg L<sup>-1</sup>) at time  $t$  (min).

## Results and Discussion

### Structure confirmation of nanocomposites

The nanocomposites with different Mnt contents were denoted MT10-1, MT5-1, and MT1-1, corresponding to mass ratios of  $m_{\text{Mnt}}:m_{\text{TiO}_2} = 10:1, 5:1, \text{ and } 1:1$ , respectively. The EDX spectra

revealed that Mnt consisted of the following elements: Al, C, Fe, K, Mg, Na, O, Si, K, and Fe (Bang Tam et al., 2021; Xinyu et al., 2021; Bang Tam et al., 2023) (Fig. 2a). MT10-1, MT5-1, and MT1-1 also had the same elements as Mnt and Ti element peaks with different intensities depending on the mass ratio (Fig. 2b–d). As the ratio of  $m_{\text{Mnt}}:m_{\text{TiO}_2}$  decreases, the wt.% of Si/Ti also decreases because the amount of Ti in the nanocomposite increases (Amit et al., 2018) (Fig. 2e). This showed that the ratio  $m_{\text{Mnt}}:m_{\text{TiO}_2}$  affected the Ti content in the Mnt /TiO<sub>2</sub> nanocomposite.

### Variation in surface morphology of Mnt and nanocomposites observed by SEM

The surface of the pure Mnt had flake particles with an average size of 400–500 nm (Jiao et al., 2018; Phetladda et al., 2018; Bang Tam et al., 2021) (Fig. 3a). After modification with TiO<sub>2</sub> at the ratio  $m_{\text{Mnt}}:m_{\text{TiO}_2} = 10:1$  (Fig. 3b; MT10-1), the Mnt surface was covered with tiny particles with a 30–45 nm diameter. These TiO<sub>2</sub> particles were randomly dispersed on the surface and between the Mnt sheets (Aydin et al., 2018; Bang Tam et al., 2021; Menelisi et al., 2021). As the mass ratio of Mnt:TiO<sub>2</sub> decreases, the density of TiO<sub>2</sub> nanoparticles on the surface and the space between the Mnt sheets increases (Fig. 3c; MT5-1). When the ratio  $m_{\text{Mnt}}:m_{\text{TiO}_2}$  was 1:1, it was almost impossible to see the Mnt sheets because the amount of TiO<sub>2</sub> nanoparticles in the nanocomposite was too great (Fig. 3d; MT1-1).

The XRD patterns of raw Mnt, TiO<sub>2</sub>, MT10-1, MT5-1, and MT1-1 (Fig. 4) revealed that TiO<sub>2</sub> nanoparticles had reflection planes belonging to the anatase phase with diffraction peaks at 25.3°, 37.9°, 47.8°, 54.3°, 55°, and 62.7°2θ, respectively, for the planes (101), (004), (200), (105), (211), and (204). The (101) reflection plane at 25.3°2θ was the characteristic peak of the anatase phase and has the greatest intensity (Bang Tam et al., 2021; Mohamed et al., 2021). Among the rutile, brookite, and anatase phases of TiO<sub>2</sub>, the anatase crystalline phase has the best photocatalytic activity (Rastgar et al., 2013; Ayoubi-Feiz et al., 2014). The (001) reflection plane of Mnt at 6.1°2θ had the greatest intensity. The raw Mnt has a basal spacing  $d_{001\text{Mnt}} = 14.5 \text{ \AA}$  (calculated by the Debye–Scherrer formula) (Mohamed et al., 2021; Peng et al., 2014). For the nanocomposites of Mnt

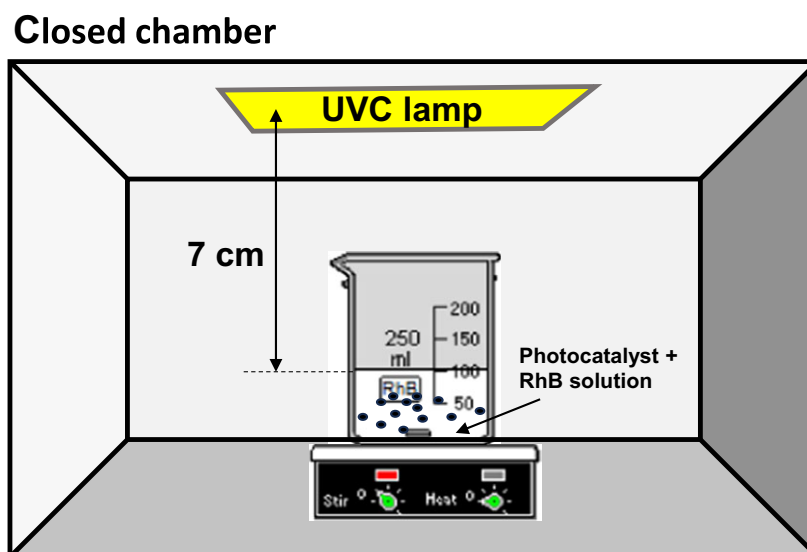
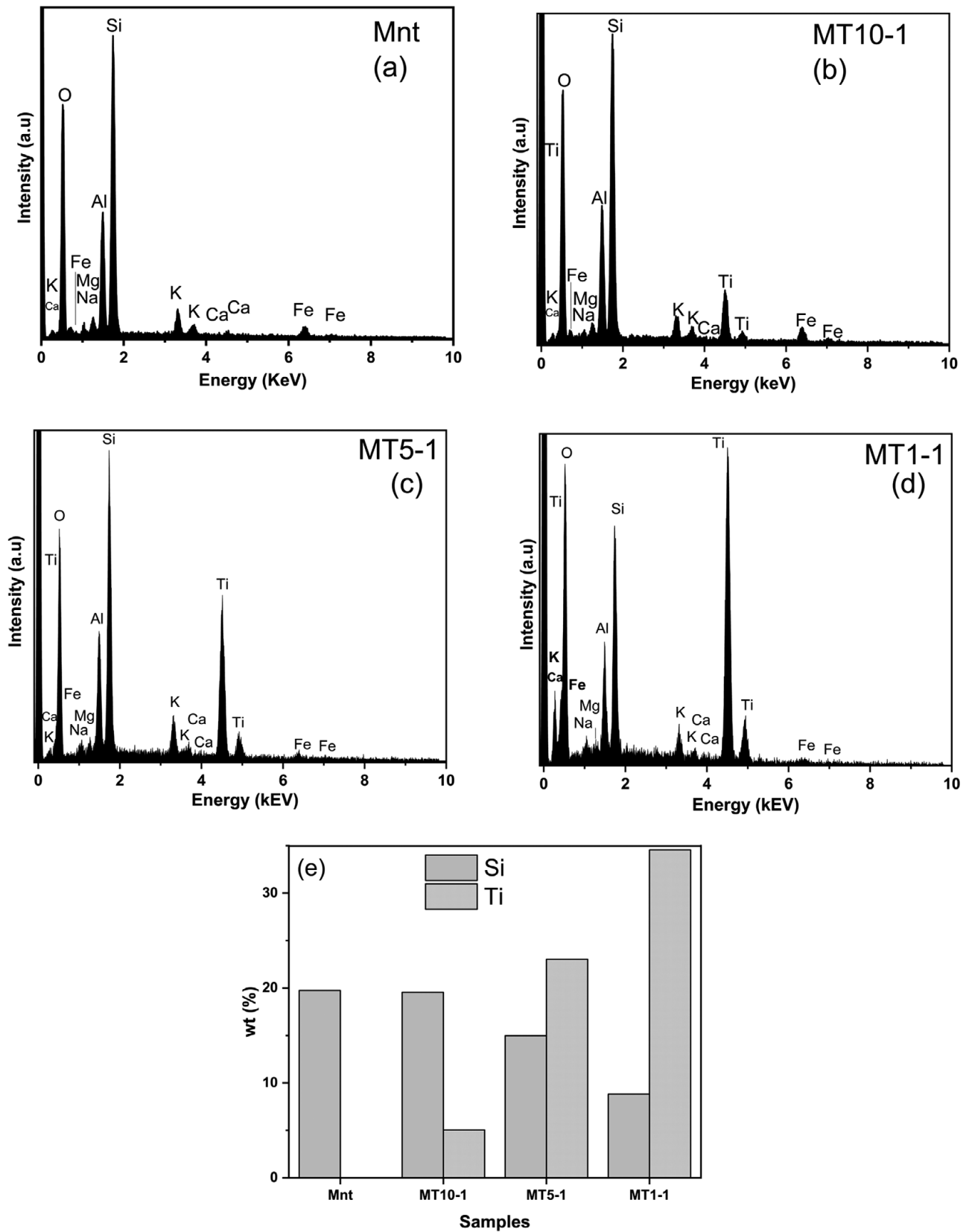


Figure 1. Experimental set-up of RhB photodegradation under the UVC light source.



**Figure 2.** EDX spectra of Mnt (a), MT10-1 (b), MT5-1 (c), MT1-1 (d), and Si/Ti (wt.%) comparison (e) for Mnt, MT10-1, MT5-1, and MT1-1.

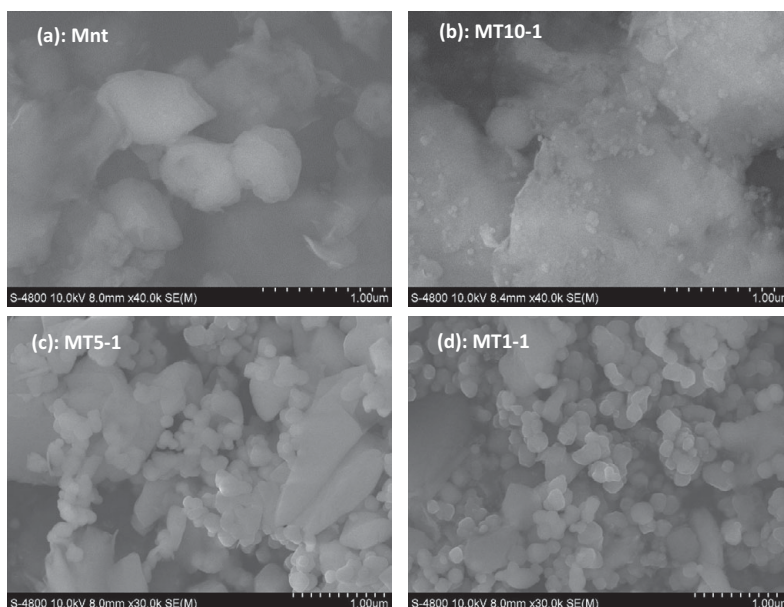


Figure 3. SEM images of raw Mnt (a), MT10-1 (b), MT5-1 (c), and MT1-1 (d).

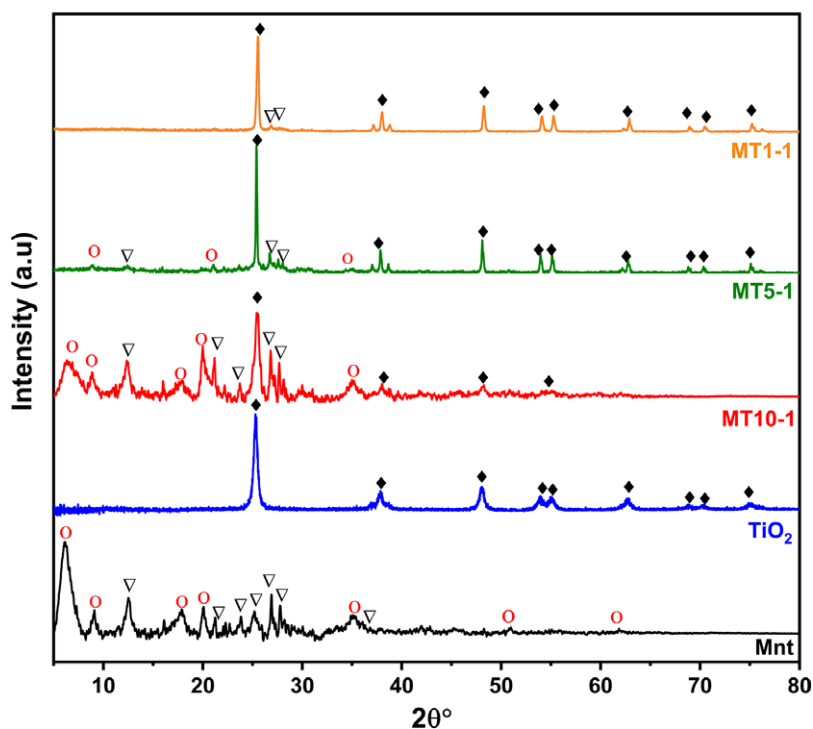
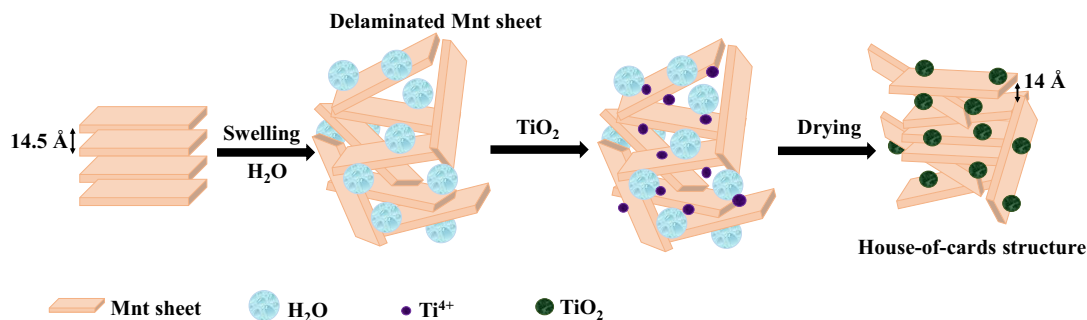


Figure 4. XRD patterns of raw Mnt, TiO<sub>2</sub>, MT10-1, MT5-1, and MT1-1 (○ = montmorillonite, ▽ = quartz, ♦ = TiO<sub>2</sub> anatase).

and TiO<sub>2</sub>, the intensity of the (001) reflection plane in the Mnt tended to decrease gradually when the ratio  $m_{\text{Mnt}}:m_{\text{TiO}_2}$  decreased. The XRD pattern of MT10-1 showed that the (001) reflection plane shifted slightly to the right at  $6.8^\circ 2\theta$  with basal spacing  $d_{001 \text{ MT10-1}} = 14 \text{ \AA}$  and some low-intensity diffraction peaks typical of TiO<sub>2</sub>. A right shift of the (001) peak was also observed in the XRD pattern of MT5-1, although very small. In addition, when reducing the Mnt content in the nanocomposites, the characteristic diffraction peaks for Mnt decreased gradually and were scarcely observed for

MT1-1, as TiO<sub>2</sub> was dominant in the MT5-1 and MT1-1 samples. This result shows that the Mnt content affected the change in the structure of the nanocomposites. During the denaturation process, TiO<sub>2</sub> nanoparticles were inserted into the space between the Mnt sheets or covered the Mnt surface, changing the distance between the Mnt sheets. Based on the analysis above, it was possible to identify the structure of the Mnt/TiO<sub>2</sub> corresponding to the house-of-cards structure (Nesmeth et al., 2003; Phetladda et al., 2018) and model it as shown in Fig. 5.





**Figure 5.** The house-of-cards Mnt/TiO<sub>2</sub> nanocomposite.

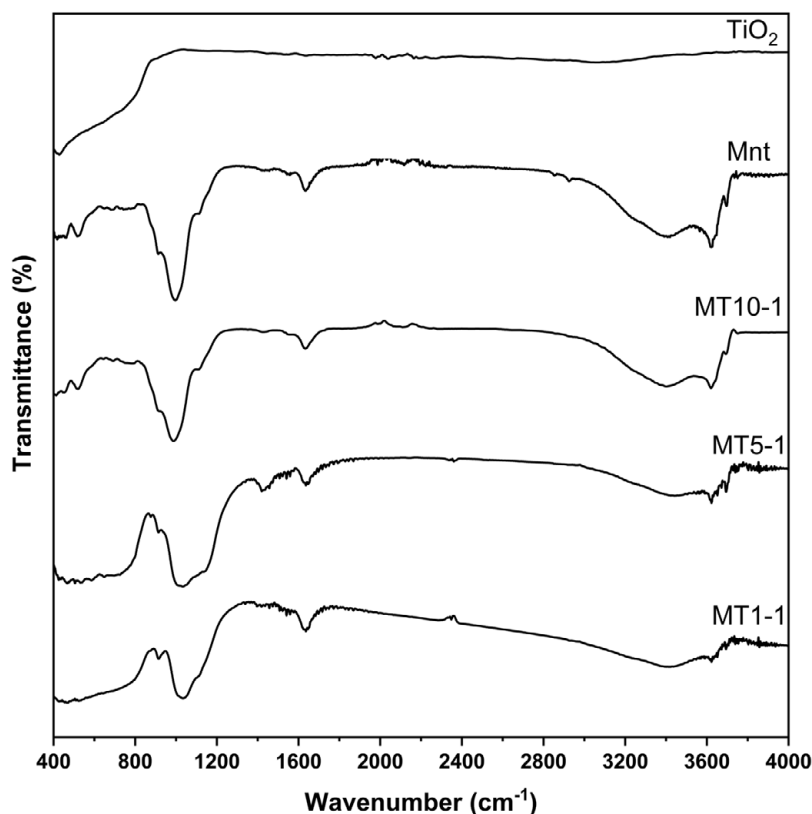


**Figure 6.** FTIR spectra of TiO<sub>2</sub>, raw Mnt, MT10-1, MT5-1, and MT1-1.

The FTIR spectra of TiO<sub>2</sub>, Mnt, MT10-1, MT5-1, and MT1-1 (Fig. 6) in the wavenumber region 400–4000 cm<sup>-1</sup> revealed that TiO<sub>2</sub> has a peak at wavenumber 480 cm<sup>-1</sup>, which corresponds to the Ti–O stretching vibration (Aydin *et al.*, 2017; Daesung *et al.*, 2019). The raw Mnt had vibrations at wavenumbers 3620 and 3420 cm<sup>-1</sup> that are attributed to the -OH symmetric stretching vibrations of water molecules in the Mnt. The absorption bands at 1640 and 1050 cm<sup>-1</sup> were attributed to the H–O–H and Si–O stretching vibrations, respectively. Bands at 912 and 785 cm<sup>-1</sup> were attributed to the Al–O stretching vibration. In addition, 530 and 472 cm<sup>-1</sup> represented the Al–O–Si symmetric stretching vibration and Si–O–Si strain vibration of Si–O–Si, respectively (Nadjia *et al.*, 2013; Aydin *et al.*, 2018). When reducing the Mnt content in the nanocomposites of Mnt and TiO<sub>2</sub>, there was a vibration competition between the characteristic peaks of TiO<sub>2</sub> and Mnt with wavenumbers 480 and 1050 cm<sup>-1</sup>, respectively. For MT10-1, because the TiO<sub>2</sub> content was minimal, only the characteristic vibrations of Mnt

can be observed. However, when the Mnt content decreased gradually, a Ti–O vibration in the 400–700 cm<sup>-1</sup> region appeared more clearly. In addition, the FTIR spectra of all samples MT10-1, MT5-1, and MT1-1 appeared in the absorption bands at 935 cm<sup>-1</sup>. This region was attributed to the Ti–O–Si bonding, which indicated that TiO<sub>2</sub> particles had been immobilized successfully into the Mnt structure to form the Mnt/TiO<sub>2</sub> nanocomposite.

The UV-Vis diffuse reflectance spectra (Fig. 7) of TiO<sub>2</sub>, Mnt, MT10-1, MT5-1, and MT1-1 showed that the absorption edges of Mnt and TiO<sub>2</sub> nanoparticles appeared at the wavelengths of 380 and 395 nm, respectively. When the Mnt content in the nanocomposite is large (MT10-1), the adsorption edge of MT10-1 is almost the same as that of Mnt. On the contrary, if the Mnt content in the nanocomposites (MT5-1 and MT1-1) is reduced, the adsorption edge of these nanocomposites behaves similarly to that of TiO<sub>2</sub> nanoparticles. In other words, a blue shift of the absorption edges toward the ultraviolet region was

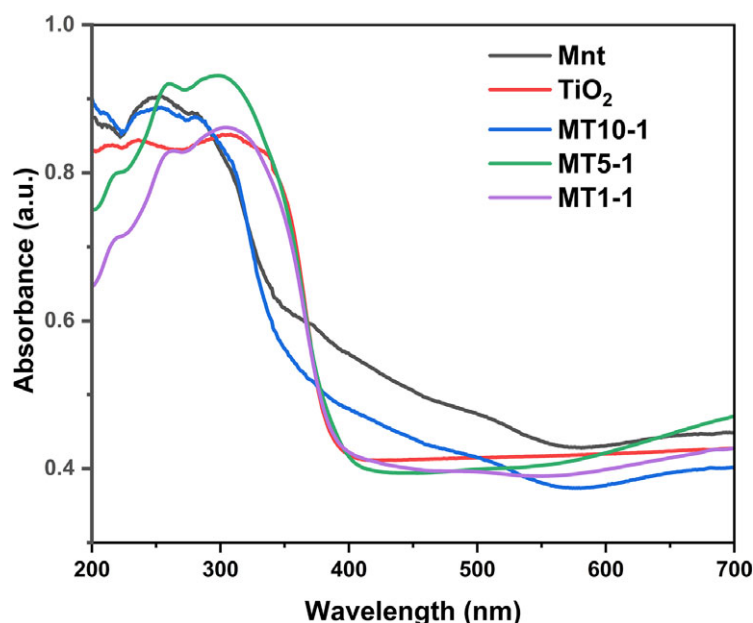


Figure 7. UV-Vis diffuse reflectance spectra of  $\text{TiO}_2$ , Mnt, MT10-1, MT5-1, and MT1-1.

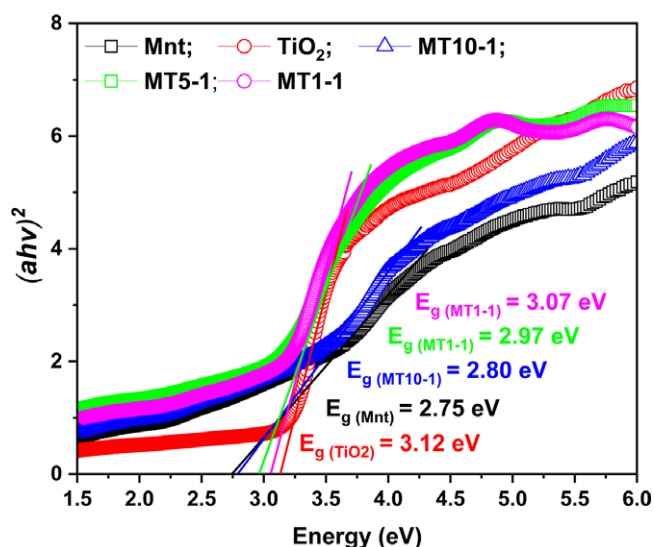


Figure 8. The band gap extrapolation lines of  $\text{TiO}_2$ , Mnt, MT10-1, MT5-1, and MT1-1.

found with increasing  $m_{\text{Mnt}}:m_{\text{TiO}_2}$  ratio due to the quantum size effect. In nanostructures, the discrete energy levels become more pronounced, and the energy band structure is altered. The energy levels become quantized, and the electronic properties of the material change. This results in changes in the material's electronic and optical properties, such as the band gap energy. The band gap energy values of  $\text{TiO}_2$ , Mnt, MT10-1, MT5-1, and MT1-1 (Fig. 8) are calculated based on Eqn 3 as 3.12, 2.75, 2.83, 2.97, and 3.07 eV, respectively. This indicates an increase in the optical band gap energy of Mnt by increasing the immobilization of  $\text{TiO}_2$  nanoparticles in the Mnt interspaces:

$$E_g = \frac{1240}{\lambda} \quad (3)$$

where  $E_g$  is the band gap energy (eV), and  $\lambda$  is the absorption edge (nm).

#### Adsorption experiment

10 mg of each material ( $\text{TiO}_2$ , Mnt, MT10-1, MT5-1, and MT1-1) was added to 100 mL of 10 ppm RhB solution and stirred under non-irradiation conditions (dark conditions) for 210 min. The variation of the  $C/C_0$  concentration ratio over time (Fig. 9) shows that  $\text{TiO}_2$  had no adsorption capacity ( $C/C_0 = 0.95$ ,  $H = 5\%$ ), while Mnt had the best RhB adsorption ( $C/C_0 = 0.38$ ,  $H = 62\%$ ). The RhB adsorption efficiency decreased gradually with the decrease in the ratio  $m_{\text{Mnt}}:m_{\text{TiO}_2}$ . These results indicated that reducing the Mnt content will reduce the adsorption of dye molecules of nanocomposites. The adsorption capacity vs time of  $\text{TiO}_2$ , Mnt, MT10-1, MT5-1, and MT1-1 was calculated according to Eqn 4 showing that the maximum adsorption capacity in 210 min of Mnt, MT10-1, MT5-1, and MT1-1 was 74.8, 59.7, 41.2, and 18.3  $\text{mg g}^{-1}$ , respectively. After 60 min, the RhB concentration from the adsorption process did not change significantly. Therefore, the adsorption-desorption equilibration time of Mnt and nanocomposites was 60 min:

$$q = \frac{(C_0 - C_t)V}{m}, \quad (4)$$

where  $q$  is the adsorption capacity ( $\text{mg g}^{-1}$ );  $V$  is the volume of solution (L);  $m$  is the amount of adsorbent (g);  $C_0$  is the concentration of the initial solution ( $\text{mg L}^{-1}$ ); and  $C_t$  is the concentration of the solution at time  $t$  ( $\text{mg L}^{-1}$ ).

#### Photocatalytic experiment

To evaluate the photocatalytic degradation of RhB, 10 mg of each material ( $\text{TiO}_2$ , Mnt, MT10-1, MT5-1, and MT1-1) was added to 100 mL of 10 ppm RhB solution and stirred under 15 W UVC irradiation for 210 min. Before the UVC excitation source was

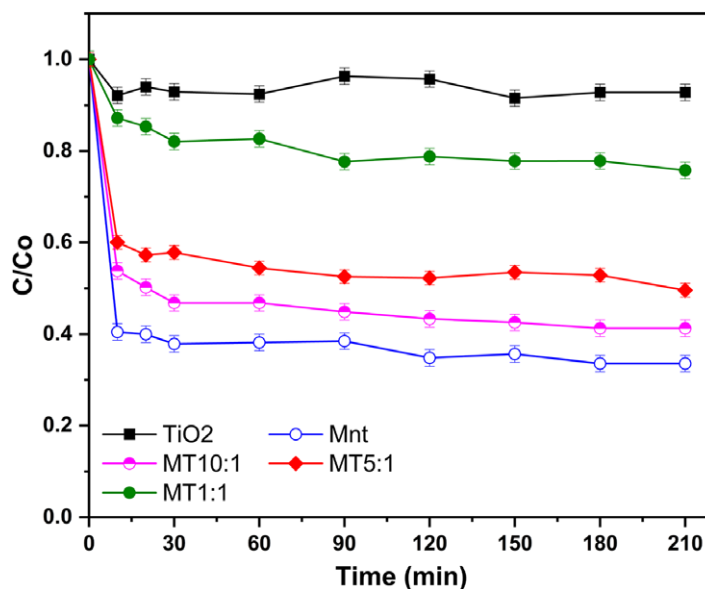


Figure 9. RhB adsorption in a dark environment by  $TiO_2$ , Mnt, MT10-1, MT5-1, and MT1-1.

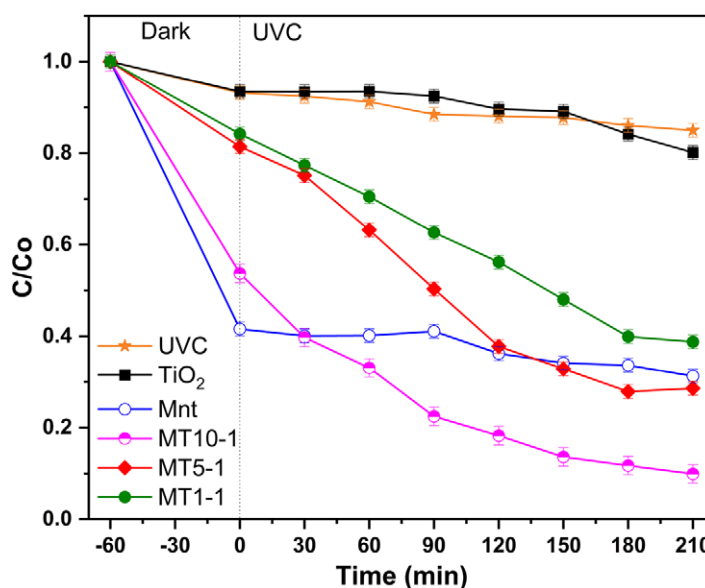


Figure 10. Photocatalytic activities of RhB by  $TiO_2$ , Mnt, MT10-1, MT5-1, and MT1-1.

switched on, the solution was stirred for 60 min to reach adsorption–desorption equilibrium. The change in concentration of the  $C/C_0$  ratio vs time (Fig. 10) suggested that the 254 nm UVC light source has excitation energy ( $E_{UVC} \approx 4.9$  eV) greater than the band gap of  $TiO_2$  ( $E_g \approx 3.2$  eV) but also not enough energy to degrade RhB ( $C/C_0 = 0.85$ ,  $H \approx 15\%$ ).  $TiO_2$  was known to be a typical photocatalytic metal oxide but had a very low photodegradation efficiency ( $C/C_0 = 0.8$ ,  $H \approx 20\%$ ). The reason was that the recombination time between  $e^+$  and  $h^-$  occurs too fast (recombination  $\approx 10^{-11}$  to  $10^{-12}$  s) (Chung *et al.*, 2011); so it did not generate many free radicals such as  $\cdot OH$  or  $\cdot O_2$  to participate in the degradation of organic dyes. Although Mnt adsorbed RhB molecules for the first 60 min when stirred in the dark ( $C/C_0 = 0.4$ ), the change in RhB concentration in the solution was insignificant after UVC irradiation ( $C/C_0 = 0.3$ ). This result demonstrated that Mnt was not photocatalytic. This small change

in concentration may be due to the continuous adsorption–desorption of RhB by Mnt during the 210 min irradiation period.

In particular, the photocatalytic effect by nanocomposites of Mnt and  $TiO_2$  increased significantly. MT10-1 had the greatest photodegradation efficiency ( $C/C_0 = 0.085$ ,  $H \approx 91.5\%$ ), MT5-1 and MT1-1 have  $C/C_0$  of 0.3 and 0.4 ( $H = 70$  and 60%), respectively. The lower the mass ratio  $m_{Mnt}:m_{TiO_2}$ , the lower the photocatalytic efficiency. This showed that Mnt influenced the photocatalytic degradation of organic dye molecules. When a semiconductor material is exposed to light, electrons are excited from the valence band to the conduction band, leaving behind positively charged holes in the valence band. These electron-hole pairs are highly reactive and can participate in redox reactions. Because of its good adsorption properties, Mnt acted as an adsorption center to capture RhB molecules in clay mineral layers and suppressed the  $TiO_2$  electron-hole pair recombination by trapping photogenerated



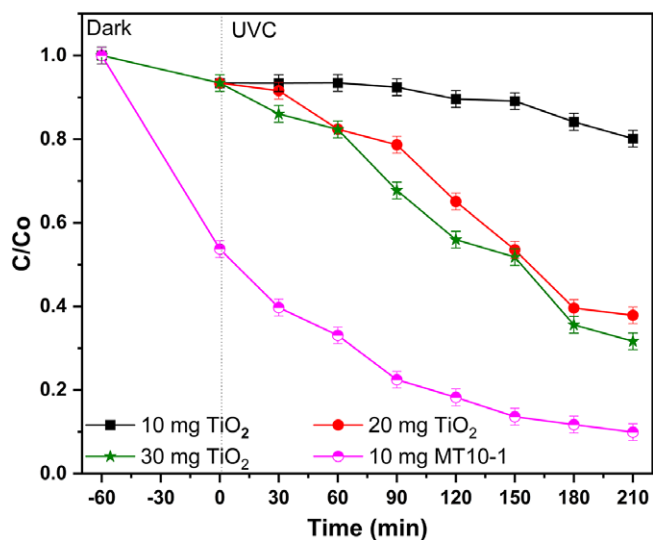


**Figure 11.** Photocatalytic activity of MT10-1 compared with those of commercial  $\text{TiO}_2$  present in various amounts.

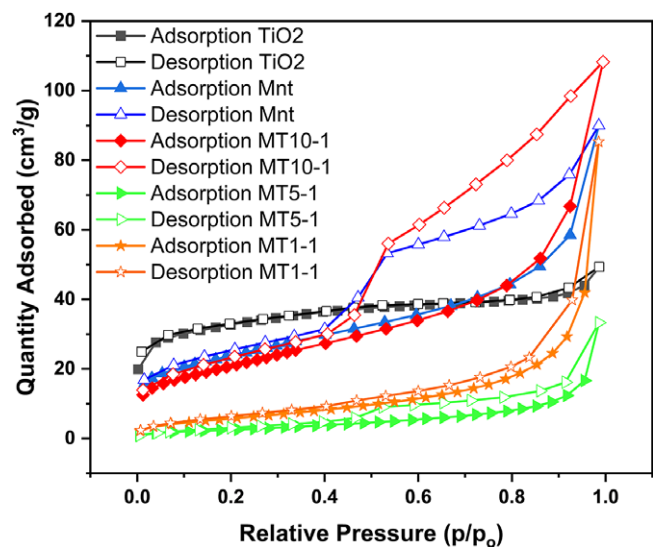


**Figure 12.**  $\text{N}_2$  adsorption-desorption isotherms of Mnt, MT10-1, MT5-1, and MT1-1.

**Table 1.** Textural characteristics of  $\text{TiO}_2$ , Mnt, MT10-1, MT5-1, and MT1-1

Sample	BET surface area ( $\text{m}^2 \text{g}^{-1}$ )	Pore diameter ( $\text{Å}$ )	Pore volume ( $\text{cm}^3 \text{g}^{-1}$ )
$\text{TiO}_2$	20.5	5.6	0.080
Mnt	83.2	40.9	0.134
MT10-1	116.8	35.0	0.180
MT5-1	35.6	32.1	0.137
MT1-1	16.1	10.2	0.054

$e^-$  into empty d orbitals of the metal in Mnt (Fangfei et al., 2009; Ling et al., 2011; Asma et al., 2021; Anh et al., 2022). Therefore, the  $\cdot\text{OH}$  or  $\cdot\text{O}_2^-$  reactive species generated from the photocatalytic reaction of  $\text{TiO}_2$  will easily react with the RhB molecules and decompose them into intermediates (Eqns 15 and 16). Oxygen

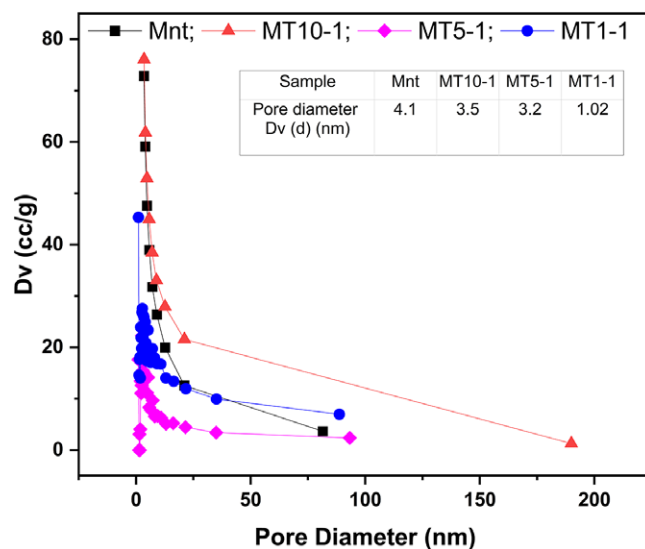


**Figure 13.** Pore-size distribution curves of Mnt, MT10-1, MT5-1, and MT1-1.

molecules in the air can be reduced by electrons from the conduction band to form superoxide radical anion ( $\cdot\text{O}_2^-$ ). This species is a potent oxidizing agent. Hydroxyl radicals ( $\cdot\text{OH}$ ) are generated through the reaction of photogenerated holes with water or hydroxide ions. They are highly reactive and can oxidize organic pollutants. The reduction of oxygen molecules by electrons from the conduction band can also lead to the formation of hydrogen peroxide ( $\text{H}_2\text{O}_2$ ). This species can act as an oxidant in photocatalytic reactions. Hydroperoxyl radical ( $\text{HO}_2\cdot$ ) can be formed through the reaction of superoxide radicals with water. It is involved in various oxidation processes. The positive holes left behind in the valence band can participate directly in redox reactions with adsorbed species on the catalyst surface. Photo-oxidation in the valence band and photo-reduction in the conduction band can occur step by step according to the following equations (Eqns 4–16) (Gao et al., 2008; Ewa et al., 2021; Kelechi et al., 2021):

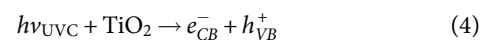


Photo-oxidation in the valence band (VB):

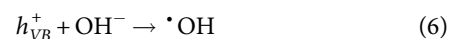
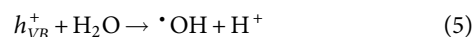
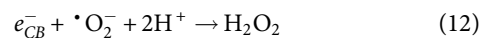
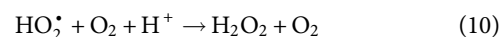
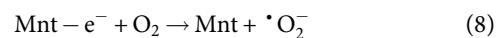
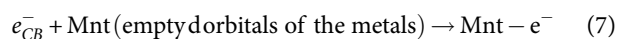
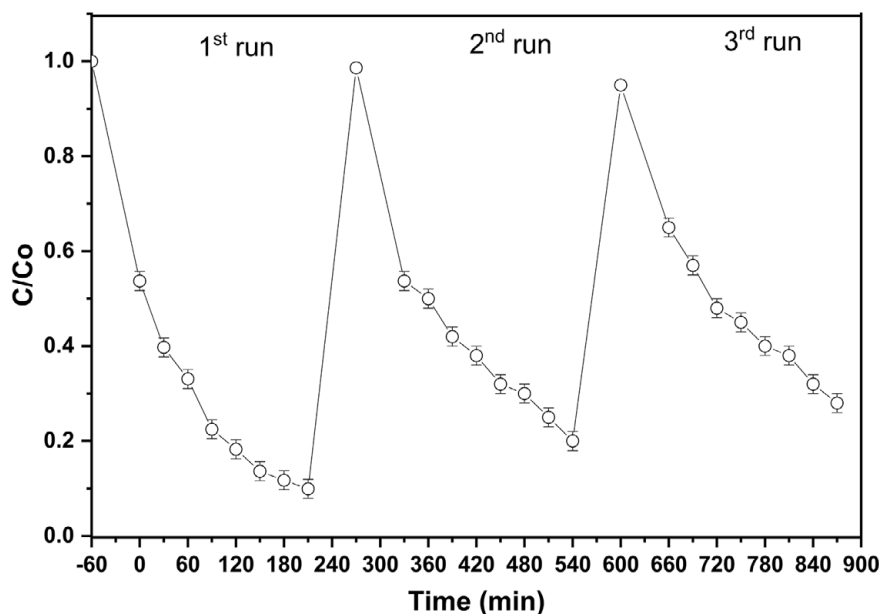


Photo-reduction in the conduction band (CB):

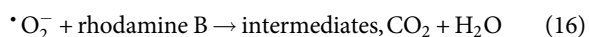
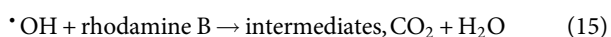
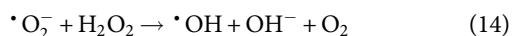




**Figure 14.** Photocatalytic activity of MT10-1 for three consecutive runs.

**Table 2.** Comparing the photocatalytic efficiency of TiO<sub>2</sub>-based photocatalysts for the degradation of rhodamine B with earlier studies

Photocatalyst	Concentration of RhB (mg L <sup>-1</sup> )	Light source (W)	Photocatalyst amount (mg)	Decomposition efficiency (%)	Exposed time (min)	Reference
<b>Mnt/TiO<sub>2</sub></b>	<b>10</b>	<b>UVC lamp (15 W)</b>	<b>10</b>	<b>91.5</b>	<b>210</b>	<b>This study</b>
B-Co/TiO <sub>2</sub> -NTs	10	UV	15	95.5	600	Hakan (2022)
In <sub>2</sub> O <sub>3</sub> /TiO <sub>2</sub> -NTs	10	Xe lamp (300 W)	—	77	120	Changren et al. (2018)
Polyaniline/graphene oxide/TiO <sub>2</sub>	5	Visible light (– W)	50	90	90	Jing et al. (2020)
TiO <sub>2</sub> /Mnt	10	Xe lamp (500 W)	150	90	120	Tao et al. (2021)
SnO <sub>2</sub> /Mnt	20	Ultrasonic probe (68 W)	500	95	120	Is et al. (2020)



To further elucidate the RhB degradation photocatalytic ability of MT10-1 nanocomposite, the TiO<sub>2</sub> content was increased from 10 to 30 mg to compare with the photocatalytic efficiency of MT10-1 (Fig. 11). Although the TiO<sub>2</sub> content in MT10-1 was only ~0.9 mg, the photocatalytic efficiency ( $H_{\text{MT10-1}}=91.5\%$ ,  $C/C_0=0.085$ ) was greater than the photocatalytic efficiency of 10 mg TiO<sub>2</sub> ( $H_{10\text{mgTiO}_2}=20\%$ ) or 20 mg TiO<sub>2</sub> ( $H_{20\text{mgTiO}_2}=62\%$ ) or even 30 mg TiO<sub>2</sub> ( $H_{30\text{mgTiO}_2}=68\%$ ). This indicated the essential role played by Mnt in the nanocomposite. In the presence of Mnt, only a small amount of TiO<sub>2</sub> was sufficient for TiO<sub>2</sub> to exhibit photocatalytic activity.

The surface textures of TiO<sub>2</sub>, Mnt, MT10-1, MT5-1, and MT1-1 were determined by the N<sub>2</sub> adsorption–desorption isotherms (Fig. 12). The BET analysis of TiO<sub>2</sub> nanoparticles shows a surface area of 20.5 m<sup>2</sup> g<sup>-1</sup>, indicating a moderate extent of surface exposure for reactions or adsorption. The pore diameter of 5.6 Å suggests very

small, possibly microporous structures, while a pore volume of 0.080 cm<sup>3</sup> g<sup>-1</sup> reflects a relatively low porosity. All the samples (Mnt and nanocomposites of Mnt) showed the hysteresis loops of type IV isotherm-desorption curves. Type IV isotherms originate from the capillary condensation in the mesopores and the interaction of molecules in the condensed state. In addition, the hysteresis loops were H4 types according to the IUPAC (the International Union of Pure and Applied Chemistry) classification. They were commonly found in microporous and medium mesopore materials. This indicated that Mnt and nanocomposites of Mnt and TiO<sub>2</sub> had open slit-shaped pores of plate-like particles. The specific surface areas of Mnt and MT10-1 were obtained from the BET measurement, and the pore size and the pore volume of Mnt and MT10-1 were calculated by the BJH method and are summarized in Table 1. Among them, the hysteresis loop of Mnt and MT10-1 has the most obvious openness. The BET surface area of MT10-1 (116.8 m<sup>2</sup> g<sup>-1</sup>) was significantly enhanced compared with that of raw Mnt (83.2 m<sup>2</sup> g<sup>-1</sup>) because of more open and less ordered pore structures (Phetladda et al., 2018). At low pressure, the adsorption of both Mnt and MT10-1 increased slowly, reflecting the adsorption of N<sub>2</sub> molecules on the inner surface of the mesoporous single-to-multilayer system. The jump in adsorption quantity at  $p/p_0=0.42$ –

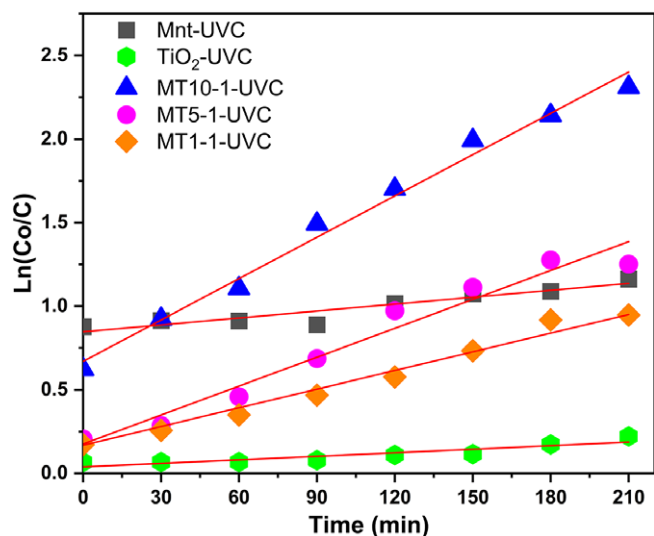


**Figure 15.** Fitting curves of the kinetic model for Mnt, TiO<sub>2</sub>, MT10-1, MT5-1, and MT1-1.

**Table 3.** Kinetic equations, reaction rate constants (K), and regression coefficients ( $R^2$ ) of photocatalytic degradation of RhB for Mnt, TiO<sub>2</sub>, MT10-1, MT5-1, and MT1-1

Sample	Kinetic equation	K (min <sup>-1</sup> )	$R^2$
Mnt	$y=0.0079x+0.7653$	0.0079	0.9662
TiO <sub>2</sub>	$y=0.0070x+0.0388$	0.0070	0.9787
MT10-1	$y=0.0824x+0.6704$	0.0824	0.9864
MT5-1	$y=0.0584x+0.6704$	0.0584	0.9576
MT1-1	$y=0.0372x+0.1685$	0.0372	0.9811

0.53 continued to increase at higher pressures, indicating a mesoporous system. In contrast, the hysteresis loops of MT5-1 and MT1-1 show that both nanocomposites have a poorly mesoporous structure. The layers of Mnt appear to be disordered due to the presence of a large amount of intercalated TiO<sub>2</sub>.

The pore-size distribution is depicted in Fig. 13. The average pore widths of Mnt, MT10-1, MT5-1, and MT1-1 are 4.1, 3.5, 3.2, and 1.02, respectively (table inset). This shows that TiO<sub>2</sub> ions reduced the pore size when they intercalated in the montmorillonite layers. The more TiO<sub>2</sub> concentration increases, the more the pore size decreases. This result is consistent with the house-of-cards structural model.

The photocatalytic stability of MT10-1 for RhB degradation was tested by running three consecutive experiments under the same conditions (Fig. 14). Photocatalysts after each experiment were centrifuged, washed, dried, and finely ground for use in subsequent experiments. After three consecutive runs, the accumulation of photocatalyst products and RhB molecules on the photocatalyst surface reduced the active sites, resulting in a decrease in photocatalytic degradation efficiency of 17%.

We compared this with other photocatalysts based on TiO<sub>2</sub> or Mnt from previous studies, in Table 2. Although each study had different preparation methods with various substances based on parameters to evaluate the effectiveness, e.g. initial RhB concentration, photocatalyst content, irradiation source power, and time exposed, the RhB degradation efficiency of MT10-1 in the present study was significantly better. The results found that the

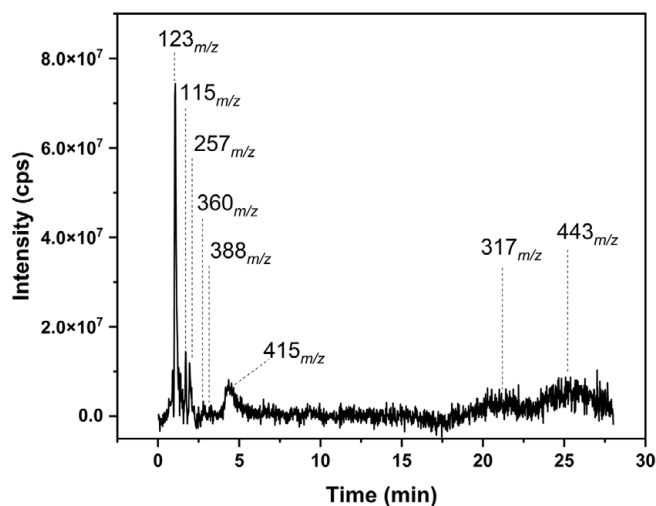


**Figure 16.** By-products of RhB degradation by MT10-1 were identified using LCMS.

less TiO<sub>2</sub>, the better the photocatalytic efficiency, and the best ratio determined in this study was  $m_{\text{Mnt}}:m_{\text{TiO}_2}=10:1$ . This mass ratio indicated an important contribution of Mnt to the RhB degradation of porous heterostructures based on Mnt and TiO<sub>2</sub>.

#### Kinetics model and intermediate products

The kinetic model of the photocatalytic degradation of RhB from Mnt and the nanocomposites of Mnt and TiO<sub>2</sub> were analyzed by the Langmuir–Hinshelwood apparent first-order kinetics equation. Figure 15 shows a plot of linear lines between  $\ln(C_0/C)$  vs time  $t$  corresponding to Mnt, TiO<sub>2</sub>, MT10-1, MT5-1, and MT1-1, demonstrating that the photodegradation was consistent with the Langmuir–Hinshelwood first-order kinetic model and this result was consistent with many previous studies (Hannatu et al., 2017; Ali et al., 2021). Table 3 summarizes the kinetics of RhB degradation over time of Mnt, TiO<sub>2</sub>, MT10-1, MT5-1, and MT1-1. The results showed that the kinematic equations had a linear form with high coefficients of determination,  $R^2$ . MT10-1 had the highest K value compared with Mnt, TiO<sub>2</sub>, MT5-1, and MT1-1, demonstrating that MT10-1 had the greatest photodegradation efficiency.

The photocatalytic degradation not only discolored RhB but also broke the bonds in the RhB molecule into smaller molecules and was identified through the LCMS method (Fig. 16). After 210 min of excitation by UVC radiation, the final solution was analyzed, and seven by-products were identified comprising the proposed scheme of RhB degradation (Fig. 17). The results showed that the initial organic dye (RhB 443<sub>m/z</sub>) (Tao et al., 2021) in the final solution was detected at just a weak intensity. First, the N-demethylation process formed nitrogen-centered reactive radicals. The by-product of this process was formed from the cleavage of the xanthene ring in the RhB molecular structure by one (or several) ethyl group, including N,N,N-diethyl-N'-ethyl rhodamine (415<sub>m/z</sub>); N,N-diethyl-rhodamine (388<sub>m/z</sub>) (Changren et al., 2018); N'-monomethyl-ethyl rhodamine (360<sub>m/z</sub>) (Hegazey et al., 2020); and N'-ethyl rhodamine (317<sub>m/z</sub>) (Sharma et al., 2019). Second, the dye chromophore structure of RhB was cleaved. During this process, the carbon centered in the RhB molecules was attacked by active species such as  $h^+$ ,  $\cdot\text{OH}$ , and  $\cdot\text{O}_2^-$  and oxidized them to the subsequent low-weight by-products (9-phenyl- 3H-xanthene (257<sub>m/z</sub>) and benzoic acid

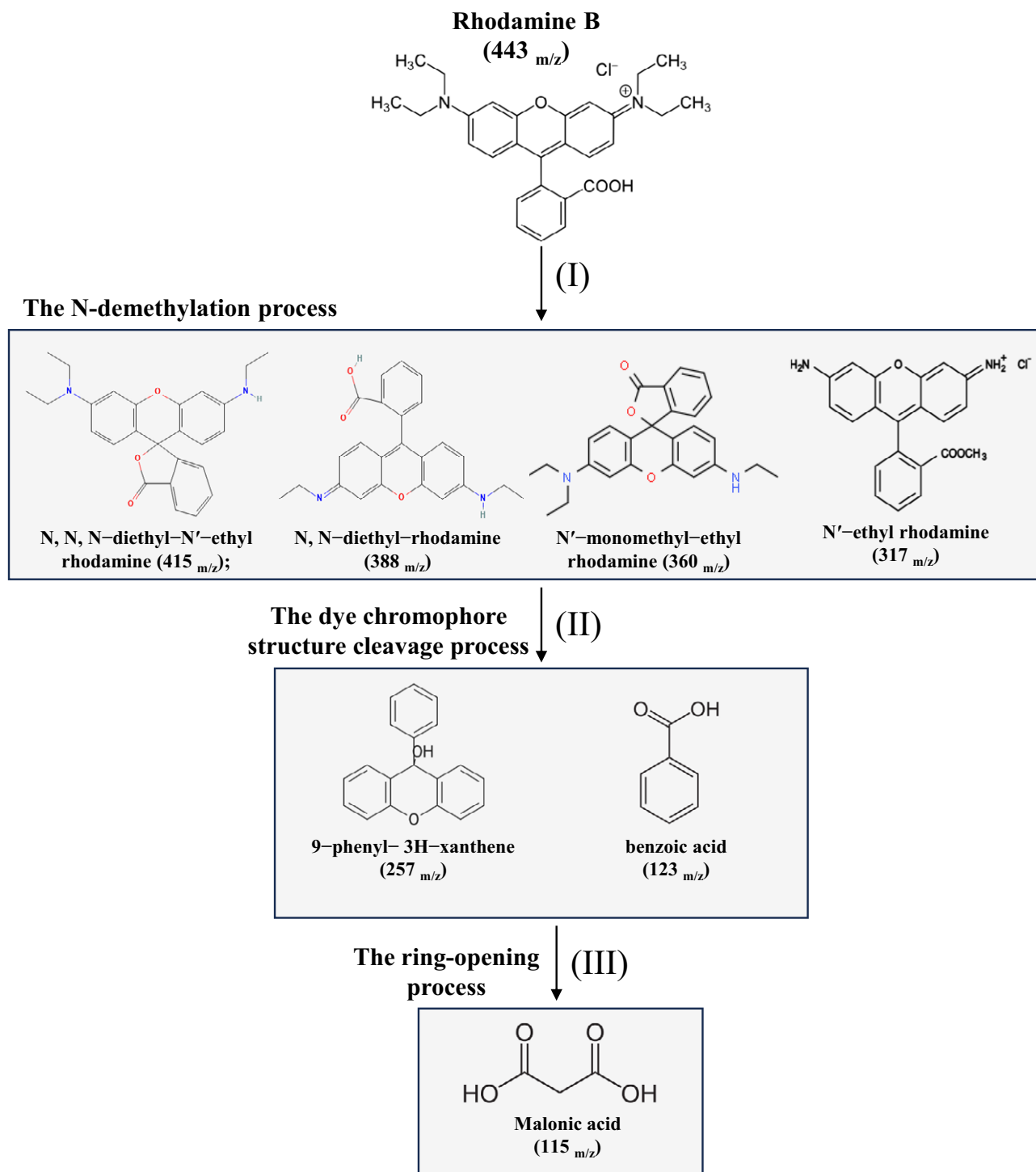


**Figure 17.** The proposed pathway of rhodamine B degradation under UVC light irradiation.

(123 $m/z$ )) (Tao et al., 2021). Finally, the ring-opening process broke the ring and formed a smaller compound, namely malonic acid (115 $m/z$ ) (Ali et al., 2018). Malonic acid is an organic acid and can undergo biodegradation through biological processes. When released into the environment, malonic acid can be metabolized by various microbial organisms that possess the necessary enzymes to break down its chemical structure. These micro-organisms use malonic acid as a carbon and energy source during their metabolic activities, leading to its degradation into carbon dioxide (CO<sub>2</sub>) and water (H<sub>2</sub>O)

or other simple and non-harmful by-products. This biodegradation process helps to reduce the concentration of malonic acid in the environment and keeps the natural ecosystem stable.

### Conclusions

In the present study, Mnt/TiO<sub>2</sub> nanocomposites with different mass ratios were synthesized by simple wet stirring and no high temperature with TiO<sub>2</sub> nanoparticles immobilized on the surface

and randomly inserted into the Mnt to form the house-of-cards structure. Investigating the influence of the ratio  $m_{\text{Mnt}}:m_{\text{TiO}_2}$  showed that the nanocomposite with the ratio  $m_{\text{Mnt}}:m_{\text{TiO}_2} = 10:1$  had the highest RhB photocatalytic efficiency ( $H_{\text{MT10-1}} = 91.5\%$ ). Due to its good adsorption properties, Mnt acts as an adsorption site and prevents recombination. The lifetime of free holes is extended to enhance the production of  $\cdot\text{OH}$  or  $\cdot\text{O}_2^-$  radicals to degrade RhB. The study shows the critical role of Mnt in improving the photocatalytic efficiency of Mnt–TiO<sub>2</sub> nanocomposites and the potential to become an advanced material in the treatment of polluted water.

**Author contribution.** Bang Tam Thi Dao: Conceptualization, Methodology, experiments, Writing- Reviewing, and Editing. Thu Loan Thi Ha: Conceptualization, Methodology, experiments, Writing- Reviewing, and Editing. Trung Do Nguyen: characterizations and operation, Writing-Reviewing, and Editing. Hon Nhien Le: Characterizations and operation, Writing, Reviewing and Editing. Tien Trung Vu: Visualization, Investigation; Huu Truong Nguyen: Visualization, Investigation; Chi Nhan Ha-Thuc: Supervision, Writing Reviewing, and Editing.

**Acknowledgements.** This work was also supported by Laboratory of Fundamental Materials Science - Faculty of Materials Science and Technology from the University of Science, VNU-HCM.

**Financial support.** This research is funded by Vietnam National University, Ho Chi Minh City (VNU-HCM) under grant number 562-2022-18-01.

**Competing interest.** The authors declare that they have no known competing financial interests or personal relationships that could have appeared to influence the work reported in this paper.

**Data availability statement.** No data available with manuscript.

## References

- Al-Tohamy, R. Ali, S.S., Li, F., Okasha, K.M., Mahmoud, Y.A.-T, Elsamahy, T., Jiao, H., Fu, Y., & Sun, J. (2022). A critical review on the treatment of dye-containing wastewater: Ecotoxicological and health concerns of textile dyes and possible remediation approaches for environmental safety. *Ecotoxicology and Environmental Safety*, 231, 113160. DOI: <https://doi.org/10.1016/j.ecoenv.2021.113160>
- Ali, A.I., Amir, P., Moslem, F., Sahand, J., & Babak, K. (2018). Photocatalytic degradation of Rhodamine B and real textile wastewater using Fe-doped TiO<sub>2</sub> anchored on reduced graphene oxide (Fe-TiO<sub>2</sub>/rGO): characterization and feasibility, mechanism and pathway studies. *Applied Surface Science*, 462, 549–564.
- Ali, H., Hajir, K., Javad, F., Mohammad, M.S., & Mehrorang, G. (2021). Heterogeneous photoelectro-Fenton using ZnO and TiO<sub>2</sub> thin film as photocatalyst for photocatalytic degradation Malachite Green. *Applied Surface Science Advances*, 6, 100126.
- Alireza, K., Kiransanc, M., Semra, K., & Mohsen, S. (2017). Photocatalytic ozonation of metronidazole by synthesized zinc oxide nanoparticles immobilized on montmorillonite. *Journal of the Taiwan Institute of Chemical Engineers*, 74, 196–204.
- Alireza, K., Murat, K., Semra, K., & Samira, A.-O. (2016). Preparation and characterization of ZnO/MMT nanocomposite for photocatalytic ozonation of a disperse dye. *Turkish Journal of Chemistry*, 40, 546–564.
- Alzain, H., Kalimugogo, V., Hussein, K., & Karkadan, M. (2023) A review of environmental impact of Azo dyes. *International Journal of Research and Review*, 10(6), 2454–2237. DOI: <https://doi.org/10.52403/ijrr.20230682>
- Amit, M., Akansha, M., & Soumen, B. (2018). Clay supported TiO<sub>2</sub> nanoparticles for photocatalytic degradation of environmental pollutants: a review. *Journal of Environmental Chemical Engineering*, 6, 6088–6107.
- Amit, M., Manisha, S., Akansha, M., & Soumen, B. (2017). Microwave treated bentonite clay based TiO<sub>2</sub> composites: an efficient photocatalyst for rapid degradation of methylene blue. *Journal of Nanoscience and Nanotechnology*, 17, 1149–1155.
- Anh, T.L., Thi Duy Hanh, L., Kuan-Yew, C., & Swee-Yong, P. (2022). Immobilization of zinc oxide-based photocatalysts for organic pollutant degradation: a review. *Journal of Environmental Chemical Engineering*, 10, 108505.
- Asma, R., Muhammad, I., Ali, S., Faiza, N., Maaz, K., Qasim, K., & Muhammad, M. (2021). Photocatalytic degradation of dyes using semiconductor photocatalysts to clean industrial water pollution. *Journal of Industrial and Engineering Chemistry*, 97, 111–128.
- Aydin, H., Alireza, K., Mehrangiz, F., & Semra, K. (2018). Photocatalytic ozonation of ciprofloxacin from aqueous solution using TiO<sub>2</sub>/MMT nanocomposite: nonlinear modeling and optimization of the process via artificial neural network integrated genetic algorithm. *Process Safety and Environmental Protection*, 116, 365–376.
- Aydin, H., Alireza, K., Semra, K., Canan, K., & Peyman, G. (2017). Sonocatalytic degradation of ciprofloxacin using synthesized TiO<sub>2</sub> nanoparticles on montmorillonite. *Ultrasonics Sonochemistry*, 35, 251–262.
- Ayoubi-Feiz, B., Aber, S., Khataee, A., & Alipour, E.J. (2014). Electrosorption and photocatalytic one-stage combined process using a new type of nanosized TiO<sub>2</sub>/activated charcoal plate electrode. *Environmental Science Pollution Research*, 21, 8555–8564.
- Bang Tam, T.D., Loan Thu, T.H., Do Trung, N., Nhien Hon, L., Truong Huu, N., & Chi-Nhan, H.-T. (2022). Montmorillonite/TiO<sub>2</sub> nanotubes could enhance the photocatalytic activity of rhodamine B degradation in the UVC region. *Science & Technology Development Journal – Natural Sciences*, 6, 2260–2270.
- Bang Tam, T.D., Thu Loan, T.H., Do Trung, N., Nhien Hon, L., Quoc Kien, L., Huu Truong, N., & Chi-Nhan, H.-T. (2023). Vietnamese montmorillonite-supported ZnO: reparation, characterization, and photocatalytic enhancement in degradation of Rhodamine B. *Kinetics and Catalysis*, 64, 390–402.
- Bang Tam, T.D., Thu Loan, T.H., Hon Nhien, L., Chi-Nhan, H.-T., Mai Loan, T.N., Patrick, P., & Dang Mao, N. (2021). Effectiveness of photocatalysis of MMT-supported TiO<sub>2</sub> and TiO<sub>2</sub> nanotubes for rhodamine B degradation. *Chemosphere* 2021, 280, 130802.
- Changren, X., Zijun, T., Cong, W., Xiaoqing, Y., Guoqing, Z., & Huageng, P. (2018). Fabrication of In<sub>2</sub>O<sub>3</sub>/TiO<sub>2</sub> nanotube arrays hybrids with homogeneously developed nanostructure for photocatalytic degradation of Rhodamine B. *Materials Research Bulletin*, 106, 197–203.
- Chengyue, Y., Chuanzhi, J., Yong, F., Feng, C., & Jianshe, H. (2022). Fast and effective uptake of mercury(II) from aqueous solution using waste carbon black-supported CuS composites and reutilization of spent adsorbent for photodegradation of rhodamine B. *Journal of Molecular Liquids*, 345, 118251.
- Chung, L. W., Yong, N.T., & Abdul, R.M. (2011). A review on the formation of titania nanotube photocatalysts by hydrothermal treatment. *Journal of Environmental Management*, 92, 1669–1680.
- Daesung, K., Garima, M., Minkyu, K., & Sanghoon, K.K. (2019). Surface modification of MMT and its effect on fatigue and fracture behavior of basalt/epoxy-based composites in a seawater environment. *Applied Surface Science*, 473, 55–58.
- Ewa, M.S. (2021). Titania-clay mineral composites for environmental catalysis and photocatalysis. *Catalysts*, 11, 1087.
- Fangfei, L., Yinshan, J., Maosheng, X., Mengmeng, S., Bing, X., & Xuehong, R. (2009). A high-stability silica–clay composite: synthesis, characterization and combination with TiO<sub>2</sub> as a novel photocatalyst for Azo dye. *Journal of Hazardous Materials*, 165, 1219–1223.
- Gao, K.Z., Xin, M.D., Fang, S.H., Xin, Y.Y., Zhou, J., Yan, J.H., & Jun, W.X. (2008). Low-temperature synthesis and photocatalytic activity of TiO<sub>2</sub> pillared montmorillonite. *Langmuir*, 24, 1026–1030.
- Ha Thuc, C.N., Grillet, A.-C., Reinert, L., Ohashi, F., Ha Thuc, H., & Duclaux, L. (2010). Separation and purification of montmorillonite and polyethylene oxide modified montmorillonite from Vietnamese bentonites. *Applied Clay Science*, 49, 229–238.
- Hakan, K. (2022). Fabrication and characterization of photoelectrode B–Co/TiO<sub>2</sub> nanotubes for effective photo electrochemical degradation of rhodamine B. *Optical Materials*, 123, 111926.
- Hannatu, A.S., Mansor, B.A., Mohd, Z.H., Nor, A.I., Aminu, M., & Tawfik, A. (2017). Nanocomposite of ZnO with montmorillonite for removal of lead and copper ions from aqueous solutions. *Process Safety and Environment Protection*, 109, 97–105.



- Hassan, A., Victor, K., Karim, H. & Mona, K. (2023). A Review of Environmental Impact of Azo Dyes. *International Journal of Research and Review*, 10 (6), 2454–2237. DOI: <https://doi.org/10.52403/ijrr.20230682>
- Hegazy, R., Abdelrahman, E., & Kotp, Y. (2020). Facile fabrication of hematite nanoparticles from Egyptian insecticide cans for efficient photocatalytic degradation of rhodamine B dye. *Journal of Materials Research and Technology*, 9, 1652–1661.
- Henrique, A.M., Andréa, R.M., & Caue, R. (2010). Synthesis of TiO<sub>2</sub>-coated CoFe<sub>2</sub>O<sub>4</sub> photocatalysts applied to the photodegradation of atrazine and rhodamine B in water. *Applied Catalysis A: General*, 382, 284–292.
- Is, F., Rico, N., Imam, S., Ganjar, F., Bambang, H.N., Azlan, K., & Oki, M. (2020). Sonocatalytic degradation of rhodamine B using tin oxide/ montmorillonite. *Journal of Water Process Engineering*, 37, 101418.
- Jiao, J., Ting, X., Yanqing, T., Jianlong, Z., Ruohua, L., Guoping, Q., & Junhui, Z. (2018). Effects of TiO<sub>2</sub> pillared montmorillonite nanocomposites on the properties of asphalt with exhaust catalytic capacity. *Journal of Cleaner Production*, 205, 339–349.
- Jing, M., Jianan, D., Yinli, D., Jiajia, Z., Liangsheng, Q., & Juanqin, X. (2020). Fabrication of PANI-TiO<sub>2</sub>/rGO hybrid composites for enhanced photocatalysis of pollutant removal and hydrogen production. *Renew Energy*, 156, 1008–1018.
- Joanna, M., Dariusz, T.M., & Beata, J. (2022). Photocatalytic degradation of sulfamethoxazole using TiO<sub>2</sub>-based materials – perspectives for the development of sustainable water treatment technology. *Science of The Total Environment*, 159122.
- Johannes, C., Emil, B., & Bambang, S. (2019). Surface modification of montmorillonite by the use of organic cations via conventional ion exchange method. *IOP Conference Series: Materials Science and Engineering*, 509, 012057.
- Ke, C., Jingyi, L., Jie, L., Yumin, Z., & Wenxi, W. (2010). Synthesis and characterization of TiO<sub>2</sub>-montmorillonites doped with vanadium and/or carbon and their application for the photodegradation of sulphorhodamine B under UV-vis irradiation. *Colloids and Surfaces A: Physicochemical and Engineering Aspects*, 360, 47–56.
- Kelechi, E.O., Kennedy, A., Kalu, S.E., & Nnamdi, E.E. (2021). Montmorillonite clay enhanced TiO<sub>2</sub> nanoparticle for photocatalytic degradation of organic pollutants: mini review. *International Journal on Pharmacy and Sciences*, 1, 33–38.
- Ling, L., Yuan, D., Huang, W., Guo, Q., Yang, J., & Yu, G. (2011). TiO<sub>2</sub>/montmorillonite nanocomposite for removal of organic pollutant. *Applied Clay Science*, 53, 272–278.
- Menelisi, C.D., Manoko, S.M.-N., & John, A.M. (2021). The use of TiO<sub>2</sub>/clay heterostructures in the photocatalytic remediation of water containing organic pollutants: a review. *Journal of Environmental Chemical Engineering*, 9, 106546.
- Miao, S., Zhimin, L., Buxing, H., Jianling, Z., Xin, Y., Jimin, D., & Zhenyu, S. (2006). Synthesis and characterization of TiO<sub>2</sub>-montmorillonite nanocomposites and their application for removal of methylene blue. *Journal of Materials Chemistry*, 16, 579–584.
- Mohamed, B., Wojciech, K., Sylwester, S., & Wojciech, Z. (2021). Effect of nanopowders (TiO<sub>2</sub> and MMT) and aramid honeycomb core on ablative, thermal and dynamic mechanical properties of epoxy composites. *Composite Structures*, 259, 113450.
- Muhammad, S., Norah, A., Lamia, B.F., Afifa, B., Walid, N., & Munawar, I. (2022). Co<sub>3</sub>O<sub>4</sub>-Bi<sub>2</sub>O<sub>3</sub> heterojunction: an effective photocatalyst for photodegradation of rhodamine B dye. *Arabian Journal of Chemistry*, 15, 103732.
- Nadjia, K.-B., Hocine, B., Hussein, K., & Bernard, D. (2013). Synthesis and characterization of TiO<sub>2</sub>-montmorillonite/polythiophene-SDS nanocomposites: application in the sonophotocatalytic degradation of rhodamine 6G. *Applied Clay Science*, 80, 56–62.
- Neelaveni, M., Santhana, P.K., Ramya, R., Sonia, T.G., & Shanthi, K. (2019). Montmorillonite/graphene oxide nanocomposite as superior adsorbent for the adsorption of rhodamine B and nickel ion in binary system. *Advanced Powder Technology*, 30, 596–609.
- Nesmeth, J., Deskany, I., Suvgh, K., Msrek, T., Klencsar, Z., Vertes, A., & Fendler, J. (2003). Preparation and structural properties of tin oxide–montmorillonite nanocomposites. *Langmuir*, 19, 3762–3769.
- Nguyen Van, H., Chu Van, H., Luu Hoang, T., Vo Nguyen, D.K., & Ha Thuc, C. (2020). The starch modified montmorillonite for the removal of Pb(II), Cd(II) and Ni(II) ions from aqueous solutions. *Arabian Journal of Chemistry*, 13, 7212–7223.
- Peng, W., Mingming, C., & Zhonghai, Z. (2014). On different photodecomposition behaviors of rhodamine B on laponite and montmorillonite clay under visible light irradiation. *Journal of Saudi Chemical Society*, 18, 308–316.
- Phetladda, P., Apisit, S., Weerapat, F., Pinit, K., & Weekit, S. (2018). Homogeneous distribution of nanosized ZnO in montmorillonite clay sheets for the photocatalytic enhancement in degradation of Rhodamine B. *Research on Chemical Intermediates*, 44, 6861–6875.
- Rania, A.-T., Sameh, S.A., Fanghua, L., Kamal, M.O., Yehia, A.-G.M., Tamer, E., Haixin, J., Yinyi, F., & Jianzhong, S. (2022) A critical review on the treatment of dyecontaining wastewater: Ecotoxicological and health concerns of textile dyes and possible remediation approaches for environmental safety. *Ecotoxicology and Environmental Safety*, 231, 113160. DOI: <https://doi.org/10.1016/j.ecoenv.2021.113160>
- Rastgar, M., Zolfaghari, A.R., Mortaheb, H.R., Sayahi, H., & Naderi, H.R. (2013). Photocatalytic/adsorptive removal of methylene blue dye by electrophoretic nanostructured TiO<sub>2</sub>/montmorillonite composite films. *Journal of Advanced Oxidation Technologies*, 16, 292–297.
- Sharma, G., Dionysiou, D., Sharm, S., Kumar, A., Al-Muhtaseb, A., Naushad, M., & Stadler, F. (2019). Highly efficient Sr/Ce/activated carbon bimetallic nanocomposite for photoinduced degradation of rhodamine B. *Catalysis Today*, 335, 437–451.
- Tammanoon, C., Varanya, S., Tanyaporn, P., Khuanjit, H., & Suwat, N. (2021). Preparation, characterization, and photocatalytic study of solvothermally grown CTAB-capped Bi<sub>2</sub>WO<sub>6</sub> photocatalyst toward photodegradation of Rhodamine B dye. *Optical Materials*, 117, 111183.
- Tao, E., Xinyu, X., & Shuyi, Y. (2021). A new synthesizing method of TiO<sub>2</sub> with montmorillonite: effective photoelectron transfer to degrade Rhodamine B. *Separation and Purification Technology*, 258, 118070.
- Tushar, M., & Bergaya, F. (2006). Organo clay mineral–melted polyolefin nanocomposites Effect of surfactant/CEC ratio. *Journal of Physics and Chemistry of Solids*, 67, 836–845.
- Xinyu Zhang, Y.G., Yuhang, L., Yingying, L., Guoying, S., & Zhenbo, Z. (2021). Efficient and stable iron-copper montmorillonite heterogeneous Fenton catalyst for removing Rhodamine B. *Chemical Physics Letters*, 776, 138673.
- Yanmin, C., Yongsheng, Y., Zhaoli, Y., Tiantian, L., Qiangshan, J., & Peng, L. (2022). Montmorillonite induced assembly of multi-element doped g-C<sub>3</sub>N<sub>4</sub> nanosheets with enhanced activity for rhodamine B photodegradation. *Applied Clay Science*, 218, 106432.
- Yonghui, Z., Baoji, M., Qiuling, C., Zhiming, B., Yange, C., & Basandorj, D. (2022). Synthesis, structure, and photocatalytic activity of TiO<sub>2</sub>-montmorillonite composites. *Catalysts*, 12, 486.
- Zhaohui, L., Nicholas, P., Joseph, R., Jianle, W., & Guocheng, L. (2018). Removal of rhodamine 6G with different types of clay minerals. *Chemosphere*, 202, 127–135.